CHEMISTRY OF MATERIALS
Cite This: *Chem. Mater.* 2019, 31, 2019−2026
Article
pubs.acs.org/cm

Large-Stokes-Shifted Infrared-Emitting InAs−In(Zn)P−ZnSe−ZnS Giant-Shell Quantum Dots by One-Pot Continuous-Injection Synthesis

Hadhi Wijaya,[†] Daryl Darwan,[†] Kang Rui Garrick Lim,[†] Tian Wang,[†] Khoong Hong Khoo,[‡] and Zhi-Kuang Tan*,[†,§]

[†]Department of Chemistry, National University of Singapore, 3 Science Drive 3, Singapore 117543
[‡]Agency for Science, Technology and Research, Institute of High Performance Computing, 1 Fusionopolis Way, #16-16 Connexis, Singapore 138632
[§]Solar Energy Research Institute of Singapore, National University of Singapore, 7 Engineering Drive 1, Singapore 117574

Supporting Information

ABSTRACT: Infrared-emitting materials with a large Stokes shift and minimal reabsorption are technologically important for luminescent solar concentrators and for bioimaging applications. Here, we describe the synthesis of new InAs−In(Zn)P−ZnSe−ZnS quaternary giant-shell quantum dots that possess efficient photoluminescence in the near-infrared region. We employ a convenient one-pot, continuous-injection approach to achieve the controlled growth of thick In(Zn)P shells around small InAs nuclei. The In(Zn)P shell absorbs strongly across the visible spectrum from 400 to 780 nm and transfers the excitation to the InAs core for emission at 873 nm, hence providing a significant Stokes shift and minimal absorption−emission spectral overlap. Density functional theory calculations reveal a conduction band delocalization and a quasi-type-II band alignment that are responsible for the significant spectral red shifts during shell growth, despite a tiny core size of ca. 3 nm. The resulting quantum dots are neutral colored, contain no regulated heavy metals, and are broadly useful in consumer optoelectronic products and biological applications.

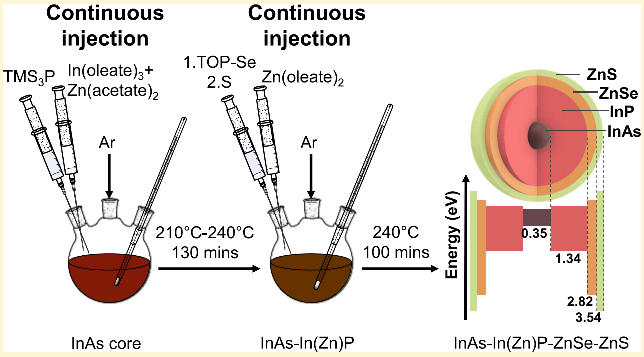

INTRODUCTION

Colloidal quantum dots (QDs) that emit in the near-infrared (NIR) region are a useful class of materials for optical communication, on-chip optoelectronics, and bioimaging applications.[1,2] In particular, the emerging field of luminescent solar concentrators (LSCs) for building-integrated photovoltaics requires NIR fluorescent emitters that possess a large Stokes shift to minimize reabsorption losses.[3−6] Meinardi et al. reported the use of a Stokes-shift-engineered giant-shell CdSe−CdS to achieve LSCs with respectable efficiencies, although the large band gap of CdS meant that only the blue photons are effectively harvested.[5] The use of toxic cadmium also limits their practical application in consumer products. Heavy metal-free copper-indium-selenide-sulfide (CISeS) quantum dots have also been employed as NIR emitters for LSCs, but possess broad emission widths of ∼200 nm that extend beyond the sensitivity of silicon solar cells.[6] Indium arsenide (InAs) quantum dots are well-known for NIR emission,[7−11] but previous implementation of the material shows significant absorption−emission spectral overlap and is therefore not immediately useful for LSCs.

RESULTS AND DISCUSSION

Here, we report a new InAs−In(Zn)P−ZnSe−ZnS quaternary giant-shell quantum dot that is designed to provide a large Stokes shift and negligible absorption−emission spectral overlap. The InAs−In(Zn)P−ZnSe−ZnS quantum dots possess increasing bulk-semiconductor band gaps of 0.35, 1.34, 2.82, and 3.54 eV (see Figure 1a) and decreasing lattice constants of 6.06, 5.87, 5.67, and 5.41 Å, respectively. The sequential decrease in lattice constants allows the lattice strain caused by mismatch to be gradually relaxed across the shell layers.[12] We designed the InAs−In(Zn)P−ZnSe−ZnS quantum dots with precursor molar ratios of 1:50:37.5:37.5. The significantly larger In(Zn)P shell absorbs strongly across the entire visible region from 400 to 780 nm and undergoes energy transfer to the InAs core to give NIR emission at 873 nm with a full width at half-maximum of 90 nm (see Figure 1b). The spectral width is contributed by a combination of size

Received: December 3, 2018
Revised: February 26, 2019
Published: February 27, 2019

DOI: 10.1021/acs.chemmater.8b05023
Chem. Mater. 2019, 31, 2019−2026

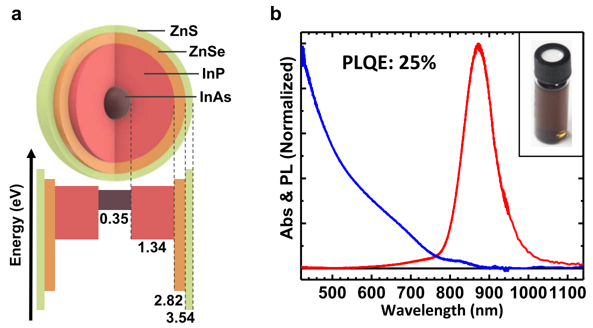

Figure 1. (a) Drawing of an InAs−In(Zn)P−ZnSe−ZnS quantum dot with the respective bulk-semiconductor band gaps. (b) Combined absorbance and photoluminescence spectra of InAs−In(Zn)P−ZnSe−ZnS quantum dots. Inset shows an image of the quantum dot solution.

dispersity and lattice disorder.[13] The quantum dots produced a photoluminescence quantum efficiency (PLQE) of 25%, which is respectable for NIR emitters. The large Stokes shift minimizes reabsorption losses and the 873 nm emission is well-matched with the photoresponsive region of silicon solar cells, hence making this quantum dot well-suited for future LSC applications. We note that this is an early, if not the first, realization of a giant-shell quantum dot design in a III−V semiconductor system.

The broad visible absorption and the invisible NIR emission give the quantum dots a practical neutral color (Figure 1b inset) that is useful for implementation in architectural or automotive windows. The material also contains no heavy metals that are regulated by the RoHS Directive and is designed to possess an extremely low arsenic content (~0.5 atom %), thereby allowing broad applications in consumer products. We note that 873 nm is also a useful wavelength for fluorescence bioimaging due to its weaker absorption and scattering by biological tissues and could therefore be potentially applied to in vivo or in vitro imaging.[14] We also tested the PL stability of the quantum dot dispersion under prolonged 405 nm (30 mW) laser photoexcitation in air and observed a minor 2% drop in the PL intensity over 6 h (Supporting Information Figure S1). The results suggest that the quantum dots possess good photostability for their intended applications.

We prepared the InAs−In(Zn)P−ZnSe−ZnS giant-shell quantum dots using a one-pot, continuous-injection methodology, and the detailed procedures are described in the Experimental Section. Briefly, we first prepared a dilute dispersion of InAs cores using indium acetate as the indium precursor, tris(trimethylsilyl)arsine (TMS_3As) as the arsenic precursor, and oleic acid as the ligand. Without purifying the InAs core, we grew a thick shell of In(Zn)P using a 50 times molar ratio of indium acetate and tris(trimethylsilyl)phosphine (TMS_3P) precursors. A 0.5 mol equivalence of zinc acetate (with respect to indium acetate) was added during the InP shell synthesis to enhance the PL of the quantum dots, as guided by previous reports.[15,16] Indeed, the absence of zinc precursors resulted in a significantly lower PLQE of 2% under the same reaction conditions (see Supporting Information Figure S2).

The In(Zn) precursor and TMS_3P precursor solutions (10 mL each) were injected into the InAs core solution at a slow rate of 0.1 mL/min using a syringe pump. The slow injection ensured that the precursor concentration in the reaction mixture remained low at all times, such that growth onto existing cores was favored compared with new nucleation events. When the speed of the injection was doubled to 0.2

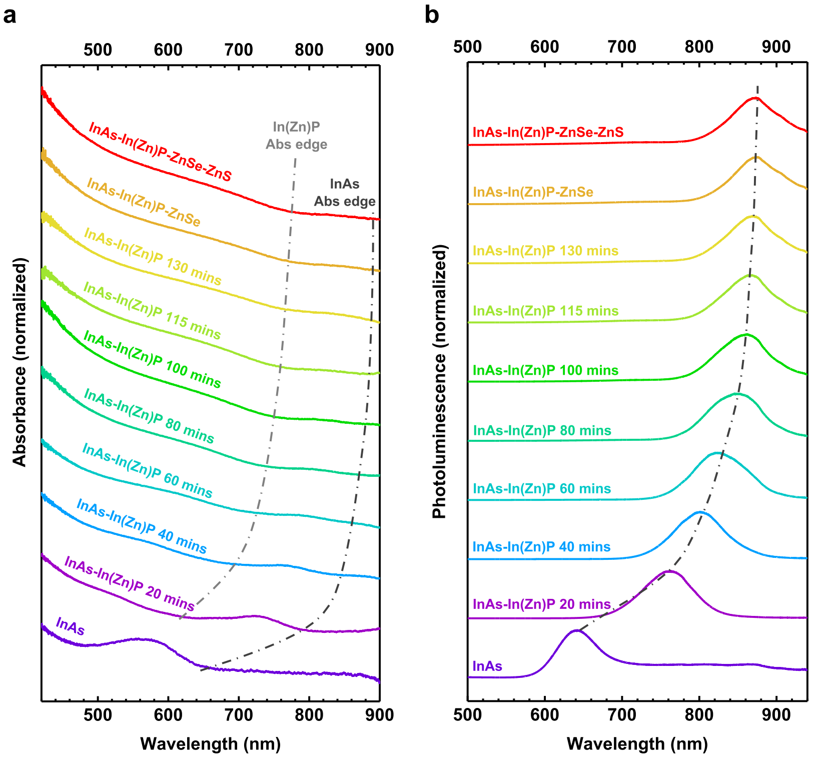

Figure 2. (a) Evolution of quantum dot absorbance during synthesis. Dashed lines trace the absorption edges of the InAs core and the In(Zn)P shell. (b) Evolution of quantum dot PL during synthesis. The dashed line traces the PL peak of the InAs core.

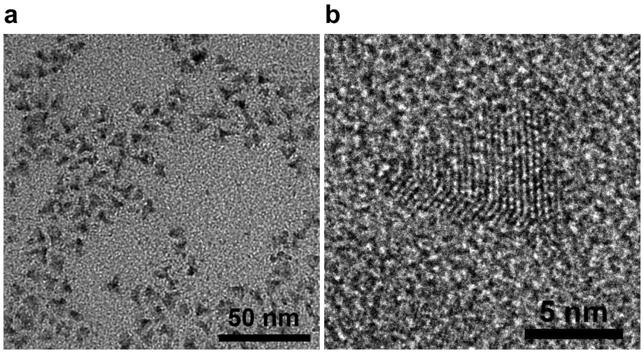

c

Element	Atomic %
In	52.3
As	0.5
P	30.5
Zn	8.6
Se	5.4
S	2.7

Figure 3. (a) Transmission electron microscopy (TEM) and (b) high-resolution TEM of InAs−In(Zn)P−ZnSe−ZnS quantum dots. (c) Table showing the atomic percentage composition of In, As, P, Zn, Se, and S, as determined by energy-dispersive X-ray (EDX) spectroscopy.

mL/min, a large shoulder peak was observed at shorter wavelengths (see Supporting Information Figure S3), indicating the nucleation and growth of new InP cores. Over the course of the injection, we raised the reaction temperature in steps from 210 to 240 °C at 33 min intervals, since higher temperatures promote the growth of larger InP quantum dots. The temperature profile of our reaction is shown in the Supporting Information Figure S4.

We tracked the progress of the reaction by extracting small aliquots from the reaction mixture at timed intervals and by measuring their UV−visible absorbance and PL characteristics. In Figure 2a, we plotted the absorbance spectra and traced the absorption edge of the InAs core and In(Zn)P shell as the layers were progressively grown. The absorption edge of the InAs core was first observed at 650 nm, but quickly shifts to 790 nm upon the first 20 min of In(Zn)P growth. This InAs absorption edge gradually red shifts to 890 nm and weakens considerably as the In(Zn)P growth continued through the continuous injection of precursors. The red shift of the InAs spectrum is a signature of the extension of the electronic wave function into the In(Zn)P shell, and the weakening of the absorption edge is due to the decreasing contributions by InAs as the 50 times larger In(Zn)P shell was grown. In the same plot, we observe the appearance of the In(Zn)P absorbance edge at 620 nm after the first 20 min of shell growth. This is followed by a progressive red shift to 780 nm and a strengthening of the absorption intensity over the remaining duration of In(Zn)P giant-shell growth. Upon completion of the In(Zn)P shell growth, additional layers of ZnSe and ZnS shells were grown through the continuous injection of the trioctylphosphine-selenium (TOP-Se) precursor solution, followed by the continuous injection of zinc acetate, oleic acid, and sulfur precursor solutions. The comparison plots in the Supporting Information Figure S5 confirm a distinct reduction in spectral overlap and an increase in Stokes shift upon the growth of the thick shell layers.

Figure 2b shows the evolution of PL spectra during the process of InAs−In(Zn)P−ZnSe−ZnS quantum dot synthesis. The InAs PL peak first appeared at 641 nm, but quickly shifted to 762 nm upon 20 min of In(Zn)P shell growth. The PL peak red-shifted further as a thicker In(Zn)P shell was grown, finally ending at 873 nm. These observations are in line with the absorbance spectral characteristics. It is worth noting that our PL measurements were performed in dilute aliquots where the QDs are independent and spatially separated. The presence of only a single emission peak in all samples therefore confirms that the In(Zn)P was grown as shells that are necessarily in close proximity to the InAs for energy transfer to occur. There was negligible nucleation and growth of independent In(Zn)P cores under our reported reaction conditions, since a separate In(Zn)P PL at a shorter wavelength was not observed. This validates the importance of a continuous injection approach,[11] whereby the In(Zn)P precursors were always maintained at a low concentration in the reaction flask to mitigate the chances of undesired In(Zn)P nucleation events. We note that it is very unlikely for the 873 nm emission to be attributed to In(Zn)P core-based QDs (without InAs), given that the highest wavelength reported for such systems is 750 nm.[17] The subsequent ZnSe and ZnS shells resulted in the enhancement of the PL intensity due to the passivation of surface defects, but caused no significant changes to the spectral characteristics.

Transmission electron microscopy (TEM) images of the InAs−In(Zn)P−ZnSe−ZnS quantum dots are shown in Figure 3a,b. The quantum dots are irregularly shaped and appear pyramidal in structure, consistent with other related InP dots that were reported in the literature.[10,18] The quantum dots have a mean size of 9.9 nm across their longest dimension, which is one of the largest sizes achieved for indium-based dots (Supporting Information Figure S9). TEM images of the InAs core, InAs−In(Zn)P, and InAs−In(Zn)P−ZnSe reveal an increase in the mean length from 2.8 to 7.6 and 9.6 nm, respectively (Supporting Information Figures S6−S8). This significant increase in the size of the dots further verifies the formation of an InAs−In(Zn)P core−shell structure. We measured the energy-dispersive X-ray (EDX) spectrum of the quantum dots and the intermediate shell layers, and tabulated their atomic content in Figure 3c and Supporting Information Figure S10. The measured atomic ratio of arsenic to phosphorous is 1:60, generally consistent with the precursor ratios. The indium to phosphorous ratio is 1.7:1, indicating an indium-rich interface with the ZnSe−ZnS shells. This is also a result of the excess indium precursors that were added during synthesis, as commonly practiced in previous works to achieve a higher PL quantum efficiency.[8,9] We also measured the EDX of the InAs−In(Zn)P dots prior to ZnSe−ZnS growth to determine whether Zn was incorporated into the InP shell. We show in the Supporting Information Figure S10 that the Zn content was insignificant at less than 3 atom %, but present nevertheless.

From the EDX data (Figure 3c), the Zn, Se, and S contents are lower compared with the precursor molar ratios, hence suggesting difficulty in growing a thick outer shell. This is likely attributed to a nontrivial lattice mismatch between the layers, as supported by the X-ray diffraction (XRD) data in Figure 4.

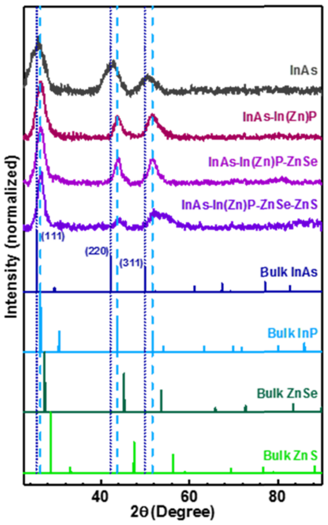

Figure 4. Background-subtracted X-ray diffraction patterns of InAs, InAs–In(Zn)P, InAs–In(Zn)P–ZnSe, and InAs–In(Zn)P–ZnSe–ZnS core–shell quantum dots at various stages of the one-pot continuous-injection synthesis. Solid vertical lines show the X-ray scattering positions and intensities of bulk zinc blende structures of InAs, InP, ZnSe, and ZnS. Vertical dotted and dashed lines are shown for the three most intense reflections corresponding to the (111), (220), and (311) planes from the bulk materials of InAs and InP, respectively.

An increase in the 2θ values of the XRD peaks toward the bulk InP material was observed after the completion of the In(Zn)P precursor injection, indicating the formation of an In(Zn)P shell overcoating the InAs core.[7] The narrowing of the XRD peaks from the InAs to the InAs–In(Zn)P quantum dots also suggests a larger crystallite size due to the formation of the In(Zn)P shell. However, a negligible shift in the XRD peaks to higher 2θ values was observed after the ZnSe and ZnS shell precursor injections, thereby reflecting their thin growth due to lattice mismatch and resulting in a modest final PLQE of 25%. Nonetheless, the observed spike in the PLQE from 10% after the In(Zn)P shell growth to 25% in the final quantum dot product despite the thin ZnSe and ZnS shells emphasizes the importance of these outer layers in enhancing the photoluminescence and photostability of the final synthesized multishell quantum dots.

We employ time-correlated single-photon counting (TCSPC) and computational modeling to gain better insight into the electronic structure of the InAs–In(Zn)P heterojunction. The PL decay curves of the InAs and the InAs–In(Zn)P quantum dots after the initial 20 min of In(Zn)P precursor injection are shown in Figure 5a. Figure 5b shows the fitted parameters of the PL decay curves using a monoexponential fit given the fact that quantum dot systems are excitonic in nature and that the defect-mediated recombination process is also expected to be pseudo-first order. The fitted curve reveals an increase in the PL lifetime (τ) from 27.7 ns in the InAs core to 44.0 ns in the InAs–In(Zn)P core–shell. We further note that even with only 20 min of In(Zn)P precursor injection, the increase in the PL lifetime was accompanied by a marked improvement in PLQE. The radiative recombination rate constant (Γ_r) increased from 0.4 μs^{-1} in the InAs core to 2.3 μs^{-1} in the InAs–In(Zn)P sample, whereas the nonradiative recombination rate constant (Γ_{nr}) decreased from 35.8 to 20.4 μs^{-1}. This indicates that the nonradiative recombination modes are suppressed, likely due to the passivation of surface defects, after the growth of the In(Zn)P shell.

Previously, the red shift observed in the InAs–In(Zn)P PL peak was reported and attributed to an extension of the electronic wavefunction during the In(Zn)P shell growth.[7,9] However, there remains a lack of evidence to validate this claim. We modeled the core–shell structure (Figure 6a) and computed the projected density of states (PDOS) of the InAs and InAs–InP core–shell structure near their Fermi levels (Figure 6b,c). A wedge model, as shown in Figure 6a, is proposed based on the TEM results to simulate the effects of shells.[19] Four different core–shell structures are considered as shown in the Supporting Information Figure S11. The InAs core is coated with three different layers of shells with the model size growing from 1 nm (InAs core) to 6 nm (InAs–InP–ZnSe–ZnS) on each side.

The band diagrams of all four structures are shown in the Supporting Information Figure S12. The band gap is 1.76 eV for the initial InAs core, and is reduced to 0.80 eV with the InP shell, 0.57 eV with InP–ZnSe shells, and 0.46 eV with InP–ZnSe–ZnS shells. The reduction in band gap is consistent with our experimentally observed red shift in the PL peak, whereby a more significant shift is contributed by InP as compared with the thinner ZnSe and ZnS shells.

The PDOS of InAs and InAs–InP near the Fermi level are shown in Figure 6b,c, and the full PDOS is shown in the Supporting Information Figure S13a,b. The broadening of peaks from the InAs core to the InAs–InP core–shell structure

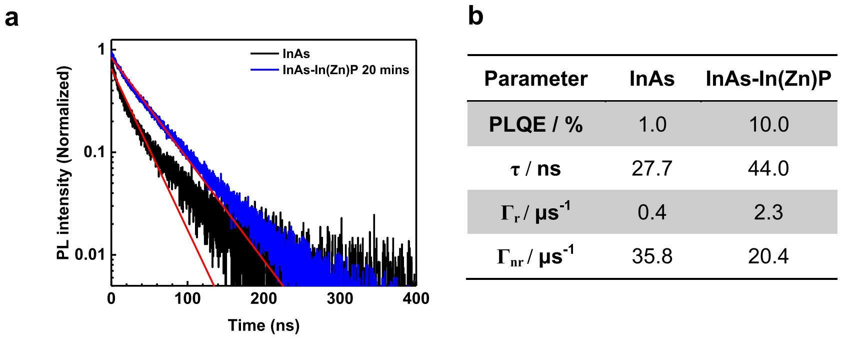

Parameter	InAs	InAs-In(Zn)P
PLQE / %	1.0	10.0
τ / ns	27.7	44.0
Γ_r / μs^{-1}	0.4	2.3
Γ_{nr} / μs^{-1}	35.8	20.4

Figure 5. (a) PL decay curves of the InAs core and the InAs–In(Zn)P quantum dots after the first 20 min of In(Zn)P precursor injection. The monoexponential decay fit for each curve is drawn in red. (b) Table showing the monoexponential decay fit parameters for both decay curves. The values of Γ_r and Γ_{nr} were estimated using eqs 1–5 in the Experimental Section.

DOI: 10.1021/acs.chemmater.8b05023

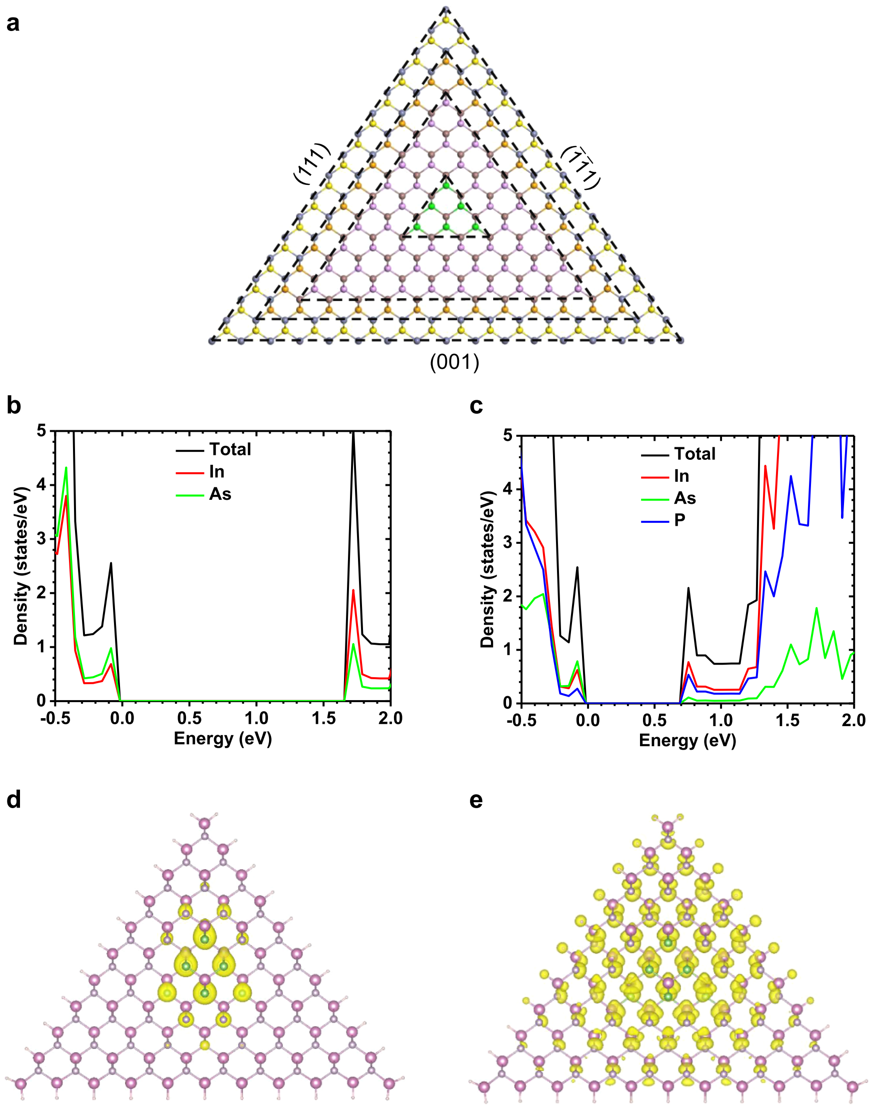

Figure 6. (a) InAs−InP−ZnSe−ZnS core−shell model with (111), ($\overline{11}1$), and (001) exposed. Dashed lines demarcate the area of each layer of materials. Ball colors represent the following: As (green), In (brown), P (purple), Se (orange), S (yellow), and Zn (gray). Pseudohydrogen atoms are not shown. (b) PDOS of the InAs core and (c) the InAs−InP core−shell near the Fermi level. All of the Fermi levels are set to 0 eV. (d) Partial charge densities of the InAs−InP core−shell for the valence band maximum (VBM) and (e) conduction band minimum (CBM) at Γ point. Isosurfaces are shown in yellow.

indicates a relaxation of the quantum confinement of electron states (Supporting Information Figure S13a,b). The InAs core in Figure 6b shows that the valence band maximum (VBM) and conduction band minimum (CBM) are equally occupied by In and As, due to the covalent nature of InAs. The InAs−InP PDOS in Figure 6c shows that the VBM edge is mainly occupied by InAs with minor contributions from InP. On the other hand, the CBM edge is 0.7 eV above the Fermi level and is mainly occupied by InP with minor contributions from InAs. Therefore, the PL red shift is mainly due to the CBM shifting toward the Fermi level after the InP shell growth. The other two shells of ZnSe and ZnS introduce a less significant impact on the band gap as compared with the InP shell and their PDOS are shown in the Supporting Information Figure S13c,d. PDOS shows that the CBM edges are still dominated by InP states after ZnSe−ZnS shell addition and hence the band gap is not significantly decreased. This agrees with the insignificant spectral shifts observed during ZnSe and ZnS growth.

The identities of the materials occupying the band edges in the InAs−InP core−shell structure were confirmed by the spatial distribution of VBM and CBM, which is visualized by the partial charge densities shown in Figure 6d,e. Figure 6d shows that the VBM is mainly localized in the InAs core area with minor delocalization to the first layer of the InP shell, whereas Figure 6e shows that the CBM is extensively delocalized beyond the first layer of the InP shell and only partially localized on InAs. This agrees with the PDOS data (Figure 6b,c) that the CBM edge is mainly occupied by InP states with minor contributions from InAs. The delocalization of the CBM into the InP shell suggests a quasi-type-II band alignment.

The partial charge densities of the InAs−InP−ZnSe and InAs−InP−ZnSe−ZnS core−shell structures are shown in the Supporting Information Figure S14c,d. The partial charge densities show that the VBM is still mainly localized on InAs with minimal leakage to InP, ZnSe, and ZnS shells, whereas the CBM is delocalized further to InP, ZnSe, and ZnS shells. The

InP−ZnSe and ZnSe−ZnS band alignments are similar to the InAs−InP quasi-type-II band alignment. Since the ZnSe and ZnS shells are thinner than the InP shell, the delocalization effects are less pronounced compared with the InP shell.

■ CONCLUSIONS

Through a delicate balance of the InAs and In(Zn)P ratio and a continuous-injection approach, we have successfully grown InAs−In(Zn)P−ZnSe−ZnS giant-shell quantum dots with a significant Stokes shift that is otherwise difficult to achieve using conventional synthetic techniques. Our calculations further reveal a quasi-type-II band alignment that is responsible for the significant spectral red shifts, and this fundamental understanding could be helpful in guiding future IR-dot design. Given that indium-based III−V semiconductor quantum dots are one of the most technologically relevant materials in the electronic display industry today and that they have a proven track record of giving bright light emission, we envision that our approach toward this similar class of heavy metal-free NIR-emitting quantum dots could facilitate their quick adoption by the industry in a range of optoelectronics, solar harvesting, and biological applications.

■ EXPERIMENTAL SECTION

Materials. 1-Octadecene (ODE, 90%, Sigma-Aldrich) was dried with activated molecular sieves in a round-bottom flask (RBF) and degassed under vacuum for 30 min before use. Octylamine (99%, Sigma-Aldrich) and oleic acid (90%, Alfa Aesar) were degassed under vacuum before use. Indium acetate (99.99%, Sigma-Aldrich), zinc acetate (99.99%, Sigma-Aldrich), and tris(trimethylsilyl)phosphine (TMS_3P, 95%, Sigma-Aldrich) were used without further purification. Tris(trimethylsilyl)arsine (TMS_3As) was synthesized according to literature procedures.[20] Tris(trimethylsilyl) arsine and tris-(trimethylsilyl)phosphine are pyrophoric and must be handled carefully in a moisture-free and oxygen-free environment. Selenium (99.99%, Sigma-Aldrich), sulfur (99.5%, Sigma-Aldrich), and trioctylphosphine (TOP, 97%, Sigma-Aldrich) were used as purchased.

InAs Core Synthesis. Indium acetate (0.01 mmol, 3 mg) and oleic acid (0.0375 mmol, 13.2 μL) were mixed with ODE (to make 4 mL) in an argon-filled 100 mL RBF. Vacuum was applied to the RBF and the mixture was heated to 60 °C for 30 min under vacuum. The mixture was heated to 210 °C and stirred for 15 min in argon to form a clear solution. TMS_3As (0.005 mmol, 1.5 μL) and octylamine (0.01 mL) were mixed with ODE (to make 1 mL) in an argon glovebox environment. The arsine solution was injected into the indium precursor solution at 210 °C over 10 s. The solution was stirred at 210 °C for 20 min to expend all precursors and complete the InAs core synthesis.

In(Zn)P Shell Synthesis. In another RBF, indium acetate (0.5 mmol, 146 mg), zinc acetate (0.25 mmol, 46 mg), and oleic acid (1.9 mmol, 666 μL) were mixed with ODE (to make 10 mL). Vacuum was applied to the RBF and the mixture was heated to 60 °C for 30 min under vacuum. The mixture was heated to 120 °C and stirred for 15 min in argon to form a clear solution. TMS_3P (0.25 mmol, 73 μL) and octylamine (0.5 mL) were mixed with ODE (to make 10 mL) in an argon glovebox environment. The indium precursor solution and phosphine precursor solution were each injected into the InAs reaction mixture, using a syringe pump, at a rate of 0.1 mL/min. The temperature was raised to 220 °C after 33 min and to 230 °C after 66 min. After complete injection at 100 min, the temperature was raised to 240 °C and the solution was stirred for another 30 min to expend all precursors and complete the In(Zn)P shell synthesis. Aliquots of the reaction were withdrawn from the reaction mixture and diluted in anhydrous hexane to track the progress of the reaction by optical absorbance and PL measurements.

ZnSe Shell Synthesis. Selenium (0.1875 mmol, 15 mg) and trioctylphosphine (TOP, 0.1875 mmol, 84 μL) were mixed with ODE (to make 3.75 mL) in an RBF at 120 °C for 30 min under an argon atmosphere to prepare the TOP-Se precursor. The precursor solution was degassed at 60 °C for 30 min under vacuum. The TOP-Se precursor solution (3.75 mL) was injected into the reaction mixture, using a syringe pump, at a rate of 0.15 mL/min. After complete injection at 25 min, the reaction mixture was stirred for another 25 min at 240 °C to expend all precursors and complete the ZnSe shell.

ZnS Shell Synthesis. Sulfur (0.1875 mmol, 6 mg) was mixed with ODE (to make 3.75 mL) in an RBF at 120 °C for 30 min under an argon atmosphere to prepare the S precursor. The precursor solution was degassed at 60 °C for 30 min under vacuum. Zinc acetate (0.1875 mmol, 34 mg) and oleic acid (0.4687 mmol, 164 μL) were mixed with ODE (to make 3.75 mL) in an RBF. Vacuum was applied to the RBF and the mixture was heated to 60 °C for 30 min under vacuum. The mixture was heated to 120 °C and stirred for 15 min in argon to form a clear zinc precursor solution. The zinc precursor solution (3.75 mL) and S precursor solution (3.75 mL) were each injected into the reaction mixture, using a syringe pump, at a rate of 0.15 mL/min. After complete injection at 25 min, the reaction mixture was stirred for another 25 min at 240 °C to expend all precursors and complete the ZnS shell.

Workup and Purification. The reaction solution was allowed to cool to room temperature. Ethanol (40 mL) was added to the reaction mixture to precipitate the InAs−In(Zn)P−ZnSe−ZnS quantum dots, followed by centrifugation of the mixture at 10 000 rpm for 5 min. The clear supernatant was carefully removed using a dropper. The addition of ethanol and the centrifugation process were repeated another three times to purify the quantum dots. The final precipitate was redispersed in hexane (20 mL) and stored for further use.

UV−Visible Absorbance Measurements. UV−visible absorbance spectra were obtained by measuring the transmitted light intensity of an Ocean Optics HL-2000 broadband light source, using an Ocean Optics Flame-T and Flame-NIR spectrometer.

Photoluminescence Quantum Yield Measurements. The photoluminescence spectra and photoluminescence quantum yield were obtained by photoexciting the samples in an integrating sphere, using a Spectra-Physics 405 nm (100 mW, CW) diode laser, and measuring the absorption and photoluminescence using a calibrated Ocean Optics Flame-T and Flame-NIR spectrometer.

Photostability Study. InAs−In(Zn)P−ZnSe−ZnS quantum dots (0.6 mg/mL in hexane in a 1 cm path-length cuvette, absorption 97%) were subjected to continuous laser irradiation (30 mW, 405 nm) for 6 h. Photoluminescence spectra were obtained at timed intervals, and the peak intensity at 873 nm was plotted against time.

Transmission Electron Microscopy (TEM) and Energy-Dispersive X-ray (EDX) Spectroscopy. TEM images were recorded using a JEOL JEM-2100F Field Emission TEM operated at 200 kV. This system is equipped with an Oxford Instruments INCA EDX. TEM samples were prepared by diluting the quantum dot solutions in hexane, followed by drop casting the solution on a copper grid.

X-ray Diffraction (XRD). Powder X-ray diffractograms were obtained using Bruker D8 ADVANCE with an X-ray source of wavelength 1.5405 Å (Cu Kα_1 line). Each XRD sample was prepared by drop casting the colloidal QD solution onto a standard single-crystal Si zero-diffraction support plate and left to dry overnight.

Time-Resolved PL Decay. Time-resolved PL decays were acquired using a time-correlated single-photon counting (TCSPC) setup (Horiba FluoroLog-3 Spectrofluorometer). Samples were excited using a 438 nm nano-light-emitting diode light source (Horiba NanoLed-440L) with a typical pulse width of 260 ps and a repetition rate of 1 MHz. The PL decay curves were fitted using the exponential equation shown in eq 1

$$I(t) = A\exp\left(-\frac{t}{\tau}\right) \tag{1}$$

DOI: 10.1021/acs.chemmater.8b05023
Chem. Mater. 2019, 31, 2019−2026

where A is the amplitude of the exponential terms, whereas τ is the PL lifetime, I is the normalized PL intensity, and t is the time.

The photoluminescence quantum efficiency (PLQE) is defined as the ratio of the radiative recombination rate constant (Γ_r) to the sum of the radiative rate constant and the nonradiative recombination rate constant (Γ_{nr}), given by eq 2

$$\mathrm{PLQE} = \frac{\Gamma_r}{\Gamma_r + \Gamma_{nr}} \tag{2}$$

The PL lifetime can also be expressed as the reciprocal of the total recombination rate constant

$$\tau = \frac{1}{\Gamma_r + \Gamma_{nr}} \tag{3}$$

Therefore, using eqs 2 and 3, we can calculate the values of Γ_r and Γ_{nr} as follows

$$\Gamma_r = \frac{\mathrm{PLQE}}{\tau} \tag{4}$$

$$\Gamma_{nr} = \frac{1 - \mathrm{PLQE}}{\tau} \tag{5}$$

First-Principle Calculation. All density functional theory calculations were performed using the Vienna ab initio simulation package.[21,22] The electron−ion interaction was described by the projector augmented wave method with an energy cutoff of 400 eV for the plane-wave basis set.[23] A 1 × 1 × 10 Monkhorst−Pack mesh was used for sampling the Brillouin zone in the structural optimization. It was increased to 1 × 1 × 32 for the study of the density of states.[24] The band structures were plotted along high-symmetry points from Γ (0, 0, 0) to X (0, 0, 0.5). The cell volume and atomic positions were optimized according to atomic forces with a threshold where the calculated force on each atom is smaller than 0.02 eV/Å. As for the exchange−correlation functional, the generalized gradient approximation of Perdew−Burke−Ernzerhof is used.[25]

The core−shell wedge models were built according to a previous report.[19] Four models with the formulas of $In_{10}As_6$, $In_{66}P_{49}As_6$, $Zn_{39}Se_{25}In_{66}P_{60}As_6$, and $Zn_{87}S_{45}Se_{25}In_{66}P_{60}As_6$ were applied to simulate the InAs cores with different layers of shells as shown in the Supporting Information Figure S11. The surfaces were passivated by pseudohydrogen atoms, that is, $q_H = 1.25e$ for each In atom and $q_H = 1.5e$ for each Zn atom. Some Se atoms at the InP−ZnSe interface were replaced with P atoms to balance the excessive negative charge between the two layers.[26] No Zn atoms were included in the InP shell during calculations to focus on the effect of the InP shell on the InAs core.

■ ASSOCIATED CONTENT

Ⓢ Supporting Information

The Supporting Information is available free of charge on the ACS Publications website at DOI: 10.1021/acs.chemmater.8b05023.

> Photoluminescence spectra, absorbance spectra, temperature profile, TEM images, EDX data, core−shell wedge models, band structures, PDOS, and partial charge densities (PDF)

■ AUTHOR INFORMATION

Corresponding Author

*E-mail: chmtanz@nus.edu.sg.

ORCID

Khoong Hong Khoo: 0000-0002-4628-1202
Zhi-Kuang Tan: 0000-0003-1399-1790

Author Contributions

This manuscript was written through contributions of all authors. All authors have given approval to the final version of the manuscript.

Notes

The authors declare no competing financial interest.

■ ACKNOWLEDGMENTS

The authors thank NUS and the Singapore Ministry of Education (MOE) for funding support (R-143-000-639-133, R-143-000-674-114, R-143-000-691-114, and R-143-000-A10-133). The authors thank Mr. Ka Yau Lee and Mr. Phai Ann Chia for assistance with TEM measurements.

■ REFERENCES

(1) Sargent, H. S. Infrared Quantum Dots. *Adv. Mater.* **2005**, *17*, 515−522.

(2) Kim, S.; Lim, Y. T.; Soltesz, E. G.; De Grand, A. M.; Lee, J.; Nakayama, A.; Parker, J. A.; Mihaljevic, T.; Laurence, R. G.; Dor, D. M.; Cohn, L. H.; Bawendi, M. G.; Frangioni, J. V. Near-infrared fluorescent type II quantum dots for sentinel lymph node mapping. *Nat. Biotechnol.* **2004**, *22*, 93.

(3) Goetzberger, A.; Greube, W. Solar energy conversion with fluorescent collectors. *Appl. Phys.* **1977**, *14*, 123−139.

(4) Bradshaw, L. R.; Knowles, K. E.; McDowall, S.; Gamelin, D. R. Nanocrystals for luminescent solar concentrators. *Nano Lett.* **2015**, *15*, 1315−23.

(5) Meinardi, F.; Colombo, A.; Velizhanin, K. A.; Simonutti, R.; Lorenzon, M.; Beverina, L.; Viswanatha, R.; Klimov, V. I.; Brovelli, S. Large-area luminescent solar concentrators based on 'Stokes-shift-engineered' nanocrystals in a mass-polymerized PMMA matrix. *Nat. Photonics* **2014**, *8*, 392−399.

(6) Meinardi, F.; McDaniel, H.; Carulli, F.; Colombo, A.; Velizhanin, K. A.; Makarov, N. S.; Simonutti, R.; Klimov, V. I.; Brovelli, S. Highly efficient large-area colourless luminescent solar concentrators using heavy-metal-free colloidal quantum dots. *Nat. Nanotechnol.* **2015**, *10*, 878.

(7) Yun-Wei, C.; Uri, B. Synthesis and Characterization of InAs/InP and InAs/CdSe Core/Shell Nanocrystals. *Angew. Chem., Int. Ed.* **1999**, *38*, 3692−3694.

(8) Battaglia, D.; Peng, X. Formation of High Quality InP and InAs Nanocrystals in a Noncoordinating Solvent. *Nano Lett.* **2002**, *2*, 1027−1030.

(9) Kim, S.-W.; Zimmer, J. P.; Ohnishi, S.; Tracy, J. B.; Frangioni, J. V.; Bawendi, M. G. Engineering InAsxP1-x/InP/ZnSe III−V Alloyed Core/Shell Quantum Dots for the Near-Infrared. *J. Am. Chem. Soc.* **2005**, *127*, 10526−10532.

(10) Xie, R.; Chen, K.; Chen, X.; Peng, X. InAs/InP/ZnSe core/shell/shell quantum dots as near-infrared emitters: Bright, narrow-band, non-cadmium containing, and biocompatible. *Nano Res.* **2008**, *1*, 457−464.

(11) Franke, D.; Harris, D. K.; Chen, O.; Bruns, O. T.; Carr, J. A.; Wilson, M. W. B.; Bawendi, M. G. Continuous injection synthesis of indium arsenide quantum dots emissive in the short-wavelength infrared. *Nat. Commun.* **2016**, *7*, No. 12749.

(12) Talapin, D. V.; Mekis, I.; Götzinger, S.; Kornowski, A.; Benson, O.; Weller, H. CdSe/CdS/ZnS and CdSe/ZnSe/ZnS Core−Shell−Shell Nanocrystals. *J. Phys. Chem. B* **2004**, *108*, 18826−18831.

(13) Janke, E. M.; Williams, N. E.; She, C.; Zherebetskyy, D.; Hudson, M. H.; Wang, L.; Gosztola, D. J.; Schaller, R. D.; Lee, B.; Sun, C.; Engel, G. S.; Talapin, D. V. Origin of Broad Emission Spectra in InP Quantum Dots: Contributions from Structural and Electronic Disorder. *J. Am. Chem. Soc.* **2018**, *140*, 15791−15803.

(14) Smith, A. M.; Mancini, M. C.; Nie, S. Second window for in vivo imaging. *Nat. Nanotechnol.* **2009**, *4*, 710.

(15) Thuy, U. T. D.; Reiss, P.; Liem, N. Q. Luminescence properties of In(Zn)P alloy core/ZnS shell quantum dots. *Appl. Phys. Lett.* **2010**, *97*, No. 193104.

(16) Pietra, F.; De Trizio, L.; Hoekstra, A. W.; Renaud, N.; Prato, M.; Grozema, F. C.; Baesjou, P. J.; Koole, R.; Manna, L.; Houtepen, A. J. Tuning the Lattice Parameter of InxZnyP for Highly Luminescent Lattice-Matched Core/Shell Quantum Dots. *ACS Nano* **2016**, *10*, 4754−4762.

(17) Xie, R.; Battaglia, D.; Peng, X. Colloidal InP Nanocrystals as Efficient Emitters Covering Blue to Near-Infrared. *J. Am. Chem. Soc.* **2007**, *129*, 15432−15433.

(18) Tessier, M. D.; Dupont, D.; De Nolf, K.; De Roo, J.; Hens, Z. Economic and Size-Tunable Synthesis of InP/ZnE (E = S, Se) Colloidal Quantum Dots. *Chem. Mater.* **2015**, *27*, 4893−4898.

(19) Zhang, S. B.; Wei, S.-H. Surface Energy and the Common Dangling Bond Rule for Semiconductors. *Phys. Rev. Lett.* **2004**, *92*, No. 086102.

(20) Wells, R. L.; Self, M. F.; Johansen, J. D.; Laske, J. A.; Aubuchon, S. R.; Jones, L. J.; et al. Tris(trimethylsilyl)arsine and lithium bis(trimethylsilyl)arsenide. *Inorg. Synth.* **2007**, *31*, 150.

(21) Kresse, G.; Furthmüller, J. Efficient iterative schemes for ab initio total-energy calculations using a plane-wave basis set. *Phys. Rev. B* **1996**, *54*, No. 11169.

(22) Kresse, G.; Furthmüller, J. Efficiency of ab-initio total energy calculations for metals and semiconductors using a plane-wave basis set. *Comput. Mater. Sci.* **1996**, *6*, 15−50.

(23) Kresse, G.; Joubert, D. From ultrasoft pseudopotentials to the projector augmented-wave method. *Phys. Rev. B* **1999**, *59*, No. 1758.

(24) Monkhorst, H. J.; Pack, J. D. Special points for Brillouin-zone integrations. *Phys. Rev. B* **1976**, *13*, No. 5188.

(25) Perdew, J. P.; Burke, K.; Ernzerhof, M. Generalized gradient approximation made simple. *Phys. Rev. Lett.* **1996**, *77*, No. 3865.

(26) Deng, H.-X.; Huang, B.; Wei, S.-H. Stable interface structures of heterovalent semiconductor superlattices: The case of (GaSb) n (ZnTe) n. *Comput. Mater. Sci.* **2015**, *98*, 340−344.

DOI: 10.1021/acs.chemmater.8b05023
Chem. Mater. 2019, 31, 2019−2026